



Deterministic single-soliton generation in a graphene-FP microresonator

ZEYU XIAO, KAN WU,* TIEYING LI, AND JIANPING CHEN

State Key Laboratory of Advanced Optical Communication Systems and Networks, Department of Electronic Engineering, Shanghai Jiao Tong University, Shanghai 200240, China

*kanwu@sjtu.edu.cn

Abstract: Dissipative Kerr solitons (DKS) in high-Q microresonators have attracted considerable attention for their broadband optical frequency combs and ultra-short pulse generation. Owing to thermal effects, complicated tuning strategies are required to generate and sustain the single-soliton state in microresonators. In this paper, we propose a novel microresonator scheme based on the Fabry-Pérot fiber resonator and single-layer graphene saturable absorber (SA) and demonstrate that this design allows deterministic single-soliton generation without frequency tuning and has strong robustness against pump perturbation. The soliton range and thermal instability of the proposed device are also discussed. This work facilitates a novel nonlinear platform connecting high-Q microresonators and conventional SA-assisted mode-locking operations.

© 2020 Optical Society of America under the terms of the [OSA Open Access Publishing Agreement](#)

1. Introduction

The temporal dissipative Kerr soliton (DKS) in microresonators exhibits an excellent performance of broadband coherent combs with low noise, and ultra-short pulses with hundred-gigahertz repetition rate [1,2], which has led to breakthroughs in several applications such as coherent communication, optical clock, frequency synthesizer, lidar, and dual-comb spectroscopy [3–7]. The DKS is a special mode-locked state that relies on the balance between the parametric gain and intracavity loss, and the balance between the Kerr nonlinearity and anomalous dispersion in the microresonators [8,9]. It has been demonstrated that microresonators can achieve ultra-high Q resonances ($\sim 10^8$) [10,11]. The high-Q factor indicates a longer photon lifetime, which can effectively extend the interaction length between the cavity and intracavity field, and lead to an ultra-low threshold of parametric oscillation [12].

To obtain DKS, the pump laser should be tuned over the cavity resonance from a short to a long wavelength with an appropriate tuning speed [9]. The single DKS state is the most desired among DKS states, since it has a single temporal pulse in each roundtrip, and possesses a smooth sech^2 -envelope. However, since the spontaneous DKS formation evolves from an uncontrollable breathing state [13], the results of frequency tuning experiments are not deterministic (e.g., number of solitons and their separation time) [14–16]. Some improvements on pump tuning strategies have been proposed to achieve deterministic single-soliton generation, including backward pump tuning [17], active feedback control [18] and the two-step “power kicking” protocol [19,20]. Methods of auxiliary laser heating [21], synchronized pulse pumping [15] and integrated heater [22] have also been demonstrated. However, frequency tuning either on the pump wavelength or resonance wavelength is always required in the above-mentioned methods. It is highly desirable to generate deterministic DKS without any frequency tuning. One possible method is the use of a phase-modulated pump laser [23], which enables the spontaneous single-soliton generation from a chirped background. Further, the studies [24,25] demonstrate the saturable absorption in a high-Q silica microtoroid, and show the possibility of obtaining robust mode-locked pulses in Kerr microresonators.

In this paper, we propose a novel Fabry-Pérot (FP) microresonator assisted by single-layer graphene (SLG) which serves as an ultrafast saturable absorber (SA). The idea is to introduce

saturable absorption into the microresonator so that the pulse shaping mechanism of the SA can help the intracavity field directly evolve to DKS. When compared to the traditional mode-locked lasers with graphene SA (e.g. [26]), the advantage of our proposed microresonator is that the gain in the microresonator arising from the Kerr nonlinearity. In contrast, the gain in traditional mode-locked lasers is due to the rare-earth-doped medium. This allows the microresonator to generate a frequency comb outside the gain spectra of rare earth elements as long as the microresonator maintains a proper anomalous dispersion. The gated intracavity tunability of optical frequency combs in a graphene based silicon nitride microresonator has also been demonstrated [27]. Here, the absorption of graphene is modelled as saturable absorption without altering its Fermi level. The Lugiato–Lefever equation (LLE) applied to the FP microresonator is derived from its equivalent coupled-mode equation including the saturable absorption effect. It is shown that when the pump frequency is set to an appropriate value, the proposed microresonator enables deterministic single-soliton generation without pump frequency tuning. Moreover, the proposed microresonator has strong robustness against pump perturbation (e.g., phase, wavelength or timing fluctuation) and can automatically recover the single-soliton state after the disappearance of perturbation. Detailed discussions on the soliton range and thermo-optic effect are also presented. This proposed microresonator connects high-Q microresonators with conventional SA-assisted mode locking and exhibits unique nonlinear dynamics. We believe that this microresonator can be a new platform for the study of nonlinear dynamics as well as a robust device for practical photonic applications.

2. Principle and model

In this study, our aim is to combine the high-Q microresonator with the well-known SA assisted mode locking. The proposed microresonator device is shown in Fig. 1. This FP microresonator uses a 1 cm long single-mode fiber (SMF) as the nonlinear medium, which is embedded in a ceramic ferrule for mechanical support and protection, similar to [15]. The left facet of the microresonator is polished and coated with high-reflection (HR) coating. The input fiber connector with anti-reflection (AR) coating is connected to this left facet through a ceramic tube. The right facet of the microresonator is polished and coated with AR coating. The SLG is sandwiched between the right facet of the microresonator and the output fiber connector with HR coating. The reflection of the HR coating and the transmission of AR coating are all assumed to be 99.9%. Since single-mode fibers have a relatively low nonlinear coefficient, they require higher pump power to excite parametric frequency conversion. Thus, synchronized pulse pumping is chosen to generate DKS more efficiently and avoid the strong thermal perturbation that appears in continuous wave pumping [14]. In contrast to synchronously pumped optical parametric oscillators (OPOs) [28,29], the combs of the pulsed pump need to match the cavity resonance to achieve a coherent build-up of intracavity fields and generate the DKS [15].

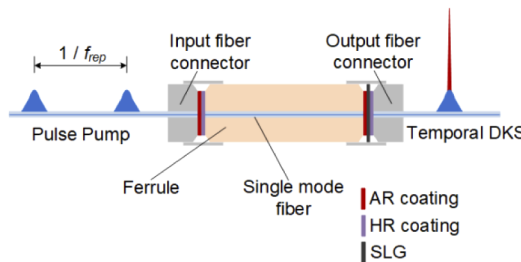


Fig. 1. Schematic diagram of the proposed SLG assisted FP microresonator.

We first establish the theoretical model for the proposed microresonator. Compared to the ring resonators, the forward and backward propagating fields in FP resonator interact and introduce an additional phase shift [15]. The earlier coupled mode model of the FP resonator is inconvenient to describe the temporal power-dependent absorption of the SLG. Hence, we derive the LLE of the FP resonator from its equivalent coupled mode equation, and transform the additional phase shift term to the temporal expression by using Parseval's theorem (Appendix A). The LLE applied to the FP microresonator is

$$t_R \frac{\partial E(t, \tau)}{\partial t} = \left[-\alpha - i\delta_0 - iL \frac{\beta_2}{2} \frac{\partial^2}{\partial \tau^2} + iL\gamma \cdot |E|^2 + 2iL\gamma P_{cav} \right] \cdot E + \sqrt{\theta} E_{in}. \quad (1)$$

where E is the field envelope inside the cavity, t_R is the round-trip time, L is the cavity length, β_2 is the second order dispersion, γ is the nonlinear coefficient, θ is the pump coupling coefficient. $\delta_0 = (\omega_0 - \omega_p)t_R$ is the pump-resonance detuning, which is caused by the mismatch between the central frequency of pulsed pump ω_p and the adjacent resonance ω_0 . P_{cav} is the average power accumulated in the cavity, given by

$$P_{cav} = \frac{1}{t_R} \int_{-t_R/2}^{t_R/2} |E|^2 d\tau. \quad (2)$$

The P_{cav} related term in Eq. (1) is the phase shift caused by the nonlinear interaction between co- and counter-propagating fields. The intracavity total loss is given by

$$\alpha = \theta + \frac{\alpha_0}{2} + \frac{\alpha_{SLG}}{2}. \quad (3)$$

where α_0 is the linear loss per roundtrip, θ is the pump coupling loss (twice that of ring resonator due to two reflective surfaces), and α_{SLG} is the power-dependent loss of the SLG. Recent studies have revealed that the photo-excited electrons of the SLG have a relaxation time about 0.1-1ps [30–32], which is comparable to the DKS duration (\sim 0.1 ps). Hence, we use the slow saturation absorption model to analyze the intracavity DKS evolution, and α_{SLG} is given by

$$\frac{d\alpha_{SLG}(\tau)}{d\tau} = -\frac{\alpha_{SLG}(\tau) - \alpha_s}{\tau_R} - \alpha_{SLG}(\tau) \frac{I(\tau)}{I_{sat}\tau_R}. \quad (4)$$

where α_s is the saturable loss, τ_R is the relaxation time, $I(\tau)$ is the instantaneous optical intensity, and I_{sat} is the saturation intensity. In the following simulation, the typical parameters of SLG are set as $I_{sat} = 2$ GW/cm², $\alpha_s = 0.023$, $\tau_R = 100$ fs and the effective mode area of SMF is set to $A_{eff} = 50$ μm^2 [30–32]. The response of the SLG with slow saturable absorption is illustrated in Fig. 2. A pump pulse with 7-fs duration and 1-kW peak power is launched to the SLG. The

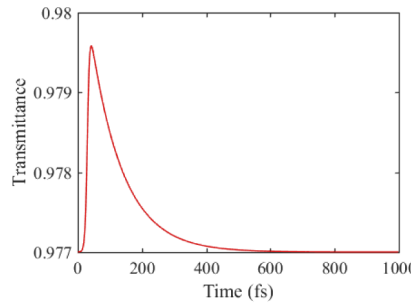


Fig. 2. The transmission of SLG after excitation by a 7-fs pump pulse.

simulated transmission change of the SLG has a slowly falling edge, which clearly indicates the accumulation effect caused by the relaxation process of graphene.

In addition, we assume that the microresonator is driven by a pulse pump with a period of t_R and a soliton profile (sech^2), given by

$$E_{in} = \sqrt{P_0} \text{ sech}(\tau/\tau_t). \quad (5)$$

where P_0 and τ_t denotes the peak power and duration time of the pulsed pump, respectively.

3. Simulations and discussions

3.1. Deterministic single-soliton generation

With the established theoretical model, the DKS generation in the proposed SLG-assisted microresonator is investigated. The following parameter values are used for the microresonator in the simulation: free spectral range (FSR) is 10 GHz; second-order dispersion β_2 is $-20 \text{ ps}^2 \text{ km}^{-1}$; nonlinear coefficient γ is $1.3 \text{ W}^{-1} \text{ km}^{-1}$; pump coupling coefficient θ is 0.1%; linear loss α_0 of FP resonator is 0.002 per roundtrip. Thus, the Q factor of microresonator is calculated to be $\sim 1.5 \times 10^7$ in the case of no graphene, which is reasonable, referred to current fabrication process [33]. The modified FP-LLE model is solved using the split-step Fourier method, and the slow SA model is solved by Runge-Kutta method with initial value of 0.023. Noise with maximum amplitude of 1×10^{-8} and random phase is added to the pump field to excite potential instabilities.

In order to illustrate the feasibility of the proposed device, the pump-resonance detuning δ_0 is fixed as 0.015, and a synchronized pulse pumping with a peak power of 40 W and duration of 1.5 ps is launched into the cavity for 8000 roundtrips. The temporal and spectral evolution results are shown in Figs. 3(a) and 3(b). After injection of the pulsed pump, the intracavity spectrum gradually broadens due to the cascaded four-wave mixing (FWM) effect. At the same time, the peak power of the intracavity pulse also increases, as shown by the red line in Fig. 3(f). At the 997-th roundtrip, the intracavity pulse reaches its highest peak power and widest spectral width during the evolution. The optical field experiences damped oscillations and eventually evolves into a stable soliton. During the evolution, no chaotic or modulation instability (MI) states appear. Figures 3(c) and 3(d) show the temporal waveform and spectral profile of the single-soliton state. It is observed that a narrow pulse is generated with a duration of 202 fs (FWHM), and its spectrum exhibits a sech^2 envelope, which verifies the generation of single soliton. It is apparent that the DKS pulse is shifted to the trailing edge of the pump pulse. This is consistent with the highest transmission of graphene occurring at the trailing edge of pump pulse due to the accumulation effect of slow saturable absorption illustrated in Fig. 2. The asymmetric shape in the time domain also results in an asymmetric spectrum in Fig. 3(d). The evolution of the intracavity power is shown in Fig. 3(e) with an obvious soliton step feature after DKS generation. Figure 3(f) shows the peak power evolution of DKS and corresponding variation of SLG saturable loss. When the peak power gradually stabilizes to 812 W, the saturation absorption loss of SLG drops from 0.023 to 0.0138. It can be observed that the SA effect of SLG in our device helps to achieve deterministic DKS generation by adjusting the intracavity loss. The SLG-induced fast-time loss dynamics $q(\tau)$ is shown in the solid line in Fig. 3(g), and the pulse profile of the soliton is shown in the dashed line. When the soliton pulse is far from the SLG, the SLG exhibits a linear loss of 0.023. When the soliton pulse reaches the SLG, the SLG exhibits a saturable loss in line with the soliton pulse profile.

We further demonstrate the contribution of SLG by comparing the intracavity pulse evolution without SLG. When the graphene SA is removed from the microresonator, two situations are considered. In case 1, graphene is removed and other parameters remain unchanged, while in case 2, an additional fixed loss is added to compensate for the difference in loss with and without graphene. In case 1, the microresonator becomes a conventional high-Q resonator. We found that

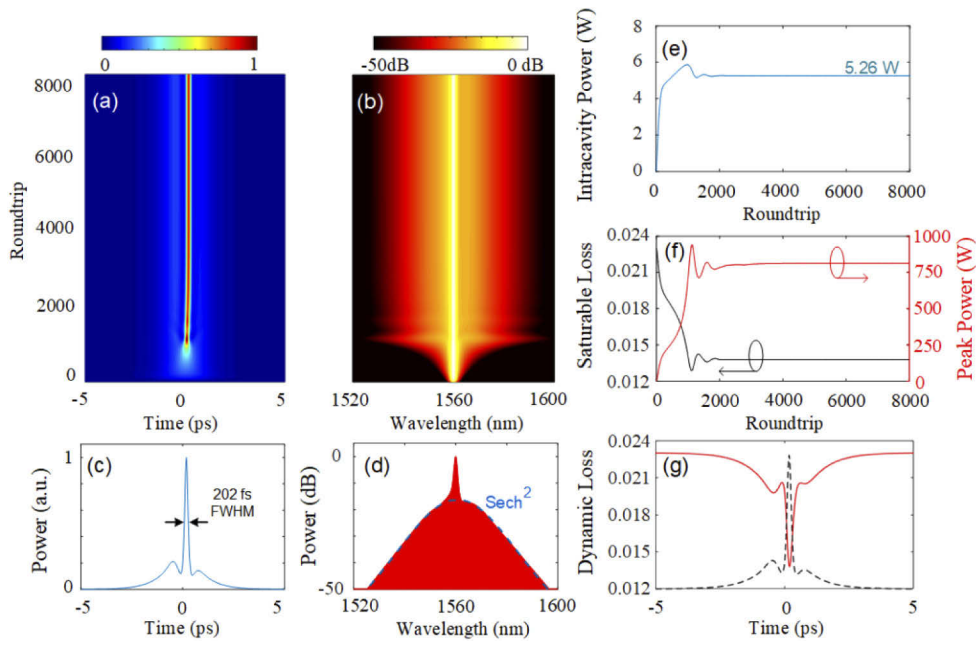


Fig. 3. (a) Temporal and (b) spectral evolution of the intracavity power at a fixed detuning of 0.015, exhibiting deterministic single-soliton generation. (c) Temporal waveform and (d) spectrum of single soliton at the final roundtrip. (e) Evolution of the intracavity power with fixed detuning of 0.015. (f) The peak power evolution of the DKS and the corresponding variation of SLG saturable loss. (g) The SLG-induced fast-time loss dynamics $q(\tau)$ after the stable soliton is generated (solid line). The dashed line shows the pulse profile of the corresponding soliton. Pump pulse: peak power 40 W, pulse duration 1.5 ps.

there exists a power and detuning region that can excite single soliton spontaneously with pulse pumping, which is similar to the results of [23]. The simulation results are shown in blue dashed lines in Fig. 4. In this simulation, the synchronized pump pulse has a peak power of 0.45 W and a duration of 1.5 ps, and the pump-resonance detuning is fixed at 0.003. The soliton evolution results in our proposed microresonator are also shown in red solid lines in Fig. 4. In this case, the pump-resonance detuning is fixed as 0.015, and the peak power of pulsed pump is set at 40 W. The intracavity graphene SA has the following two effects: Firstly, it equivalently introduces an intracavity loss and reduces the Q factor of the microresonator. Secondly, the saturable absorption of graphene increases the pumping efficiency of spontaneous soliton generation. The incorporation of the SLG of course reduces the pumping efficiency, but meanwhile, it increases the absolute value of soliton peak power because the spontaneous single-soliton generation needs to meet the bistable condition ($\delta_0 > \sqrt{3}\alpha$) and a low-Q microcavity allows higher power of the lower branch and thus higher peak power of the generated soliton, as shown in red curves in Fig. 4.

Then, we discuss the case 2, and show that the saturable absorption of graphene further compensates the pumping efficiency loss by introducing a power dependent loss. Figures 5(a)–5(c) summarize the waveforms, spectra, and power of the microresonator at four different loss values $\alpha_{FIX} = 0.017, 0.018, 0.019$ and 0.023 (maximum loss of single-layer graphene). The pump detuning is fixed at 0.015 (no frequency sweeping) and the peak power and pulse duration of the pump pulse are fixed at 40 W and 1.5 ps, which are the same as those for the microresonator with SLG. For the loss value $\alpha_{FIX} = 0.023$, no spectral broadening can be observed and the waveform in time domain is the same as the pump pulse. For the loss value $\alpha_{FIX} = 0.017\sim0.019$, spectral

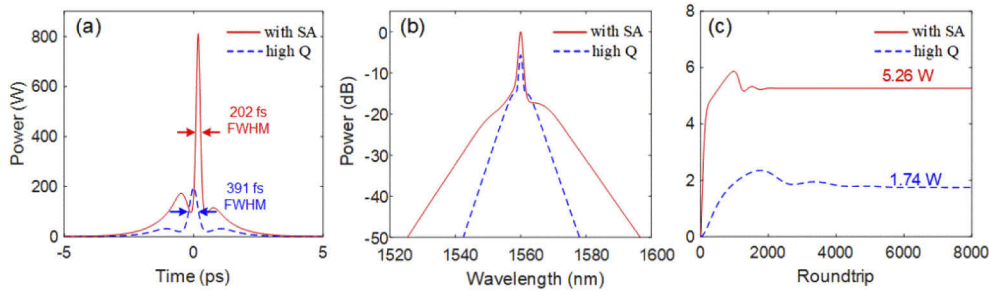


Fig. 4. Comparison of (a) temporal waveforms, (b) spectra and (c) power evolution between the microresonator with SA graphene and without SA graphene. In the case of with no SA, Pump pulse: peak power 0.45 W, pulse duration 1.5 ps and detuning is 0.003. In the case of with SA, Pump pulse: peak power 40 W, pulse duration 1.5 ps and detuning is 0.015.

broadening and pulse-like waveforms can be observed in the time domain. However, even in the best condition of $\alpha_{FIX} = 0.018$, the microresonator with SLG shows better performance, as shown in Fig. 5(d). The waveform from the microresonator with graphene SA has narrower pulse duration, higher peak power and lower pedestal. In Fig. 5(e), the spectrum from the microresonator with graphene also shows a broader spectrum width and lower pump power peak, which indicates a more efficient pump conversion. Figure 5(f) shows the intracavity power evolution with and without SLG ($\alpha_{FIX} = 0.018$). The power of the microresonator with SLG is lower because more pump power is converted to the DKS, as shown in Fig. 5(e).

The allowed detuning range for deterministic soliton generation is then investigated. When the pulsed pump has a peak power of 40 W and duration of 1.5 ps, the microresonator can achieve

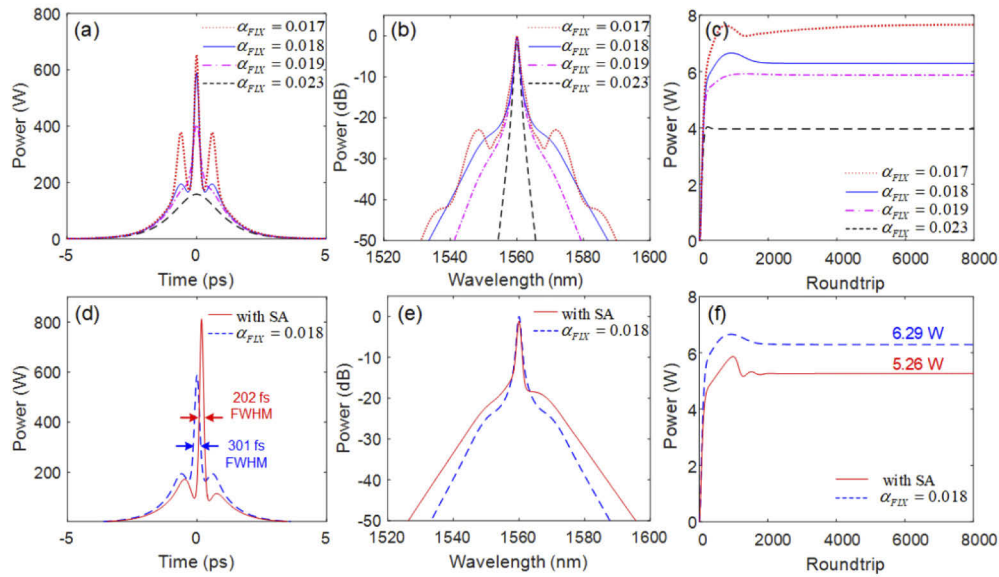


Fig. 5. Simulation results of (a) temporal waveforms, (b) spectra and (c) power evolution when graphene is replaced by a fixed loss $\alpha_{FIX} = 0.017, 0.018, 0.019$ and 0.023 respectively. Comparison of (d) temporal waveforms, (e) spectra and (f) power evolution between the microresonator with graphene and the microresonator with a fixed loss $\alpha_{FIX} = 0.018$. Pump pulse: peak power 40 W, pulse duration 1.5 ps and detuning is 0.015.

deterministic generation of single soliton in the detuning range of 0.014 to 0.016. The temporal waveforms for the allowed detuning values are shown in Fig. 6(a). The corresponding peak power and pulse duration of soliton are shown in Fig. 6(b). For a fixed pump power, deterministic solitons can be generated over a certain detuning range. In addition, larger detuning leads to higher peak power and narrower pulse duration.

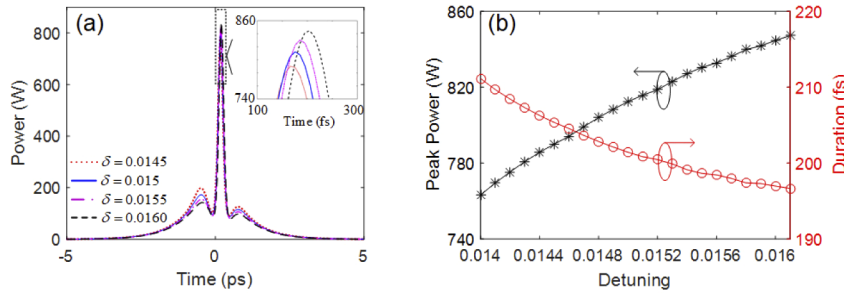


Fig. 6. (a) Temporal waveforms at detuning of 0.0145, 0.015, 0.0155 and 0.016 respectively. At these detuning values, the microresonator can achieve deterministic soliton generation. Inset: an enlarged view of the pulse peak. (b) The corresponding soliton peak power and duration at different values of the detuning. Pump pulse: peak power 40 W, pulse duration 1.5 ps.

3.2. Soliton range and Hopf bifurcation

The previous simulation has illustrated that the intracavity field of the proposed microresonator can directly evolve into soliton state at a proper fixed detuning and power. However, for a larger fixed detuning, direct DKS generation can no longer be achieved. This is because larger detuning leads to a decrease in the intracavity power and breaks the balance between parametric gain and cavity loss. In this section, we will discuss the DKS dynamics at a larger detuning range.

In an externally driven microresonator, the soliton range (δ_0 , P_{in}) is used to characterize the existence region of a single soliton. Here, we use the split-step Fourier method to solve the FP-LLE, and obtain the soliton range of the SLG-assisted microresonator, as shown in Fig. 7(a). We observe that the soliton range can be divided into four regions. Region I is the non-DKS state, region II is the one-DKS state, region III is the breathing state, and region IV is the MI state. It should be noted that region III is a special quasi-state area. The single DKS oscillates in region III meanwhile retaining its localized spatial structure [34]. The boundary between regions II and III is associated with Hopf bifurcation in externally CW-driven damped nonlinear Schrödinger equation [35]. The soliton solution loses its stability on crossing the Hopf bifurcation. The Hopf bifurcation originates from the Gavrilov–Guckenheimer (GG) point [36], and has been experimentally observed in fiber resonances [34] and Si₃N₄ microresonators [37]. Figures 7(b) and 7(c) show the intracavity spectral and power evolution at a fixed detuning of 0.025. The boundary of each region can be clearly identified.

3.3. Influence of the thermo-optic effect

When the microresonator is externally driven by the laser pump, the dissipated power gets converted to heat, changes the refractive index of the waveguide refractive index due to the thermo-optic effect and red-shifts the resonance of the microresonator [22]. Hence, the external pump laser is tuned across the resonance from the blue to the red side to increase the DKS thermal stabilization time in the conventional pump tuning method.

In our proposed microresonator, the central frequency of the pulsed pump is fixed at the proper red-detuned region to directly evolve into the single DKS. When the thermo-optic effect

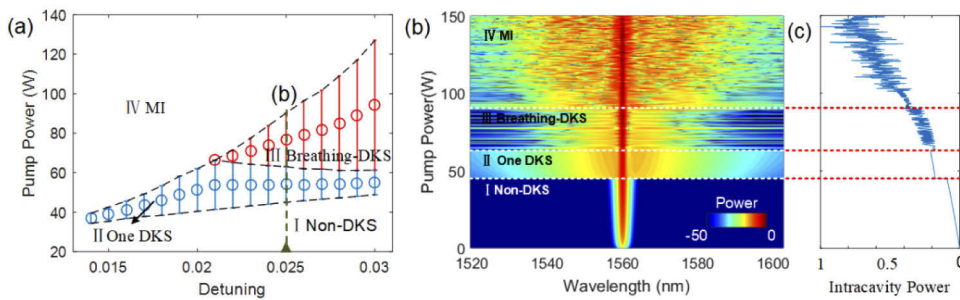


Fig. 7. (a) Soliton range of the proposed SLG assisted microresonator. Evolution of (b) optical spectrum and (c) intracavity power with increasing pump power at a fixed detuning of 0.025.

is considered, the pump-resonance detuning can no longer be regarded as a constant. The accumulation of intracavity power and heat can disturb the detuning between the resonance and the pump frequency and suppress the stable DKS generation. Thus, the initial detuning should be tuned to larger values to ensure that the thermally shifted detuning is still located in the single DKS region.

We study the influence of the thermo-optic effect in the proposed microresonator by including thermal detuning in the modified LLE. Subsequently, Eq. (1) can be rewritten as

$$t_R \frac{\partial E(t, \tau)}{\partial t} = \left[-\alpha - i(\delta_0 + \delta_\Theta) - iL \frac{\beta_2}{2} \frac{\partial^2}{\partial \tau^2} + iL\gamma \cdot |E|^2 + 2iL\gamma P_{cav} \right] \cdot E + \sqrt{\theta} E_{in}, \quad (6)$$

$$\frac{d\delta_\Theta}{dt} = -\frac{\delta_\Theta}{\tau_0} + \xi P_{cav}. \quad (7)$$

where $\delta_\Theta = (\omega_\Theta - \omega_0)t_R$ is the thermal detuning, and ω_Θ is the thermal induced cavity resonance shift, τ_0 is the thermal response time, and ξ is the coefficient describing the detuning shift caused by the intracavity power P_{cav} [14]. $\xi \propto \Lambda \alpha_0 / C$, depends on the thermo-optic coefficient Λ of material, the transmission loss α_0 , and the heat capacity C of microresonator. Since the waveguide of SMF in the microresonator exhibits ultra-low transmission loss, the thermal dissipation induced heat power is relatively small. In addition, the SLG used in the microresonator has an extremely high thermal conductivity [38], and can transfer the intracavity heat from fiber core area to its periphery, helping in alleviating thermal detuning. In the following simulation, we use $\tau_0 = 100$ ns, and $\xi = -0.5 \times 10^4 \text{ W}^{-1}\text{s}^{-1}$ to simulate the influence of the thermo-optic effect in our microresonator. The intracavity temporal and spectral evolutions are shown in Figs. 8(a) and 8(b), respectively, while the instantaneous waveform and spectrum profile after thermal stabilization are shown in Figs. 8(c) and 8(d). The corresponding intracavity power and detuning evolutions are presented in Figs. 8(e) and 8(f). The stabilized single DKS is generated after ~ 6000 roundtrips at the intracavity power of 5.1 W, and the pump-resonance detuning is thermally shifted from 0.018 to 0.0154. Since the final stabilized detuning is still at the single DKS region, the thermo-optic effect does not hinder the direct generation of the soliton. Unlike the conventional tuning method in which the DKS is evolved from the pulse-like noise state and the intracavity field experiences a huge thermal perturbation, the DKS in our proposed microresonator is directly excited from the fixed-detuning pulsed pump without going through chaotic and breathing states. Thus, there is less thermal perturbation in the cavity, which helps in building up thermal stabilization.

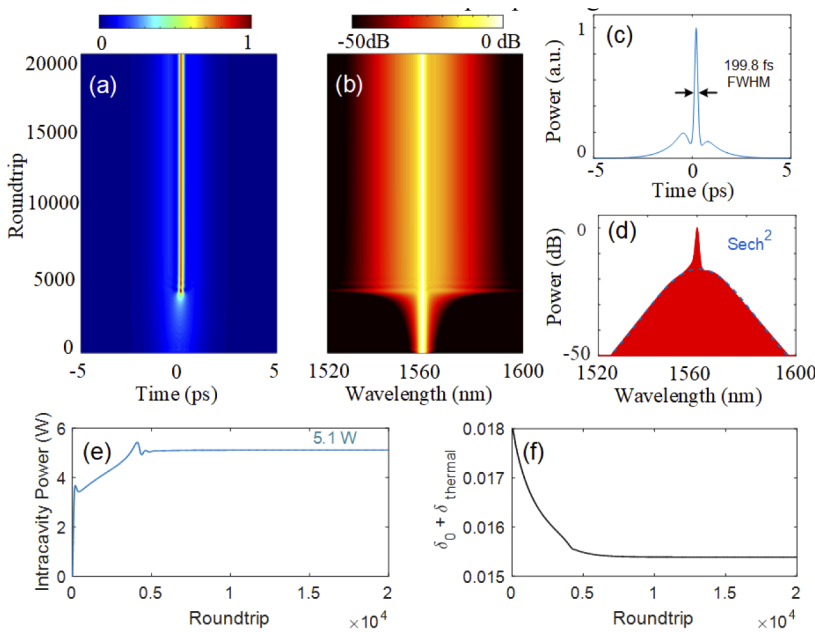


Fig. 8. (a) Temporal evolution and (b) spectral evolution with the increase of round trips. (c) Temporal waveform and (d) spectrum of the single soliton after thermal stabilization. Evolution of (e) intracavity power and (f) detuning. Pump pulse: peak power 40 W, pulse duration 1.5 ps.

3.4. Robustness to pump perturbation

Since DKS generation in microresonators is based on the double balance between gain and loss, nonlinearity and dispersion, the soliton stability is highly sensitive to pump perturbation [21]. For conventional DKS generation in microresonators, the frequency tuning process must be repeated to produce the DKS state when it disappears due to the pump perturbation. An obvious advantage of our SLG assisted microresonator is its robustness against pump perturbation. In this section, we demonstrate the self-recovery of the DKS in our device when it is temporarily suppressed by the pump perturbation.

Figure 9(a) shows the DKS evolution when a pump frequency jitter occurs at the 2000th roundtrip. The DKS disappears due to the frequency jitter (detuning increased by 0.1 with a duration of 10 ns) and re-builds itself successfully after the disappearance of frequency jitter in another ~2000 roundtrips. Figure 9(d) exhibits the phase evolutions $\Delta\Phi_\mu(t)$ of different modes in response to this frequency jitter. $\Delta\Phi_\mu(t)$ is defined as the change of phase $\Phi_\mu(t)$ of μ -th mode, i.e., $\Delta\Phi_\mu(t) = \Phi_\mu(t) - \Phi_\mu(0)$. Here, the 100th, 200th, 300th and 400th modes are monitored. The phases of the different modes are all recovered.

Figure 9(b) shows the DKS evolution when a π phase jump occurs at 2000th roundtrip. It can be clearly observed that the DKS re-builds itself after another ~2000 roundtrips. The corresponding phase evolutions of $\Delta\Phi_\mu(t)$ are shown in Fig. 9(e). The phases at different modes are again recovered after the re-establishment of DKS.

Similarly, when a 10-ps timing shift of pump pulse occurs, the DKS can also recover itself after another ~2000 roundtrips, as shown in Fig. 9(c). The corresponding phase evolutions $\Delta\Phi_\mu(t)$ are shown in Fig. 9(f). The recovered phases in Fig. 9(f) have a linear phase difference compared to the original values owing to the timing shift of the DKS.

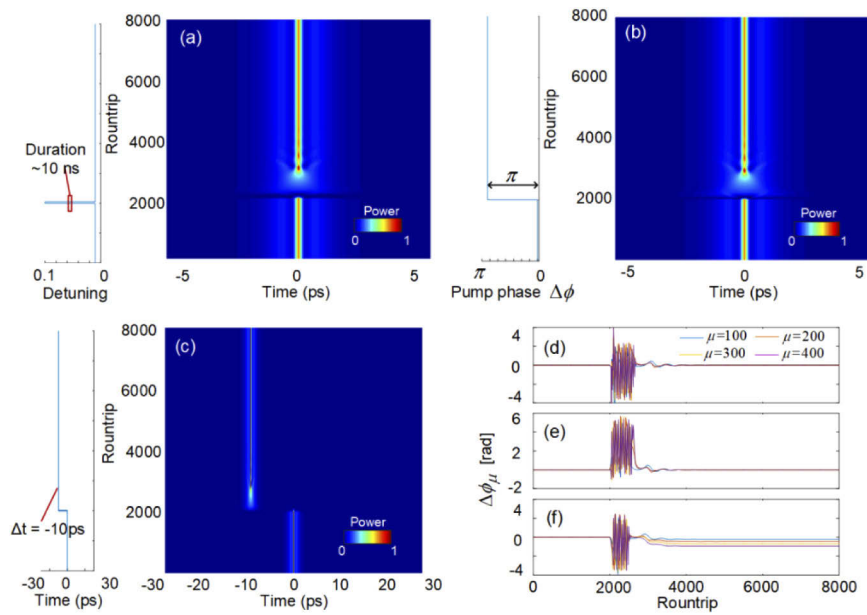


Fig. 9. Self-recovery of DKS state in the proposed microresonator with (a) 10-ns long detuning perturbation, (b) pump phase jump of π and (c) 10-ps timing shift of pump pulse at 2000th roundtrip. (d)–(f) The phase evolutions of different modes when the pump perturbation is introduced. Pump pulse: peak power 40 W, pulse duration 1.5 ps.

3.5. Influence of relaxation time

The parameters of graphene play an important role in our proposed microresonator. We numerically investigate the effect of the relaxation time while fixing other parameters ($I_{sat} = 2$ GW/cm², $\alpha_s = 0.023$). The simulation results are shown in Fig. 10(a). We find that the peak power of the soliton decreases significantly as the relaxation time increases. This is because the longer relaxation time increases the response time, which, in turn, decreases the peak transmittance of the SLG, as shown by Fig. 10(b). In Fig. 10(c), when the relaxation time τ_R changes from 10 fs to 500 fs, the pulse duration increases from 189 fs to 402 fs, and the peak power of soliton decreases from 864 W to 478 W. At the same time, the temporal location of the soliton also changes with the relaxation time, which is reported in Fig. 10(d). The DKS begins to deviate from the central position of pulsed pump, and reaches its maximum shift at $\tau_R = 350$ fs as the relaxation time increases. Further increases in the relaxation time cause the DKS to move back towards the central position of the pump. This is because when the relaxation time approaches zero ($\tau_R \rightarrow 0$), Eq. (4) is equivalent to the fast-saturated absorber model, and the DKS tends to generate at the location of the highest power. When the relaxation time approaches infinity ($\tau_R \rightarrow \infty$), the loss of the SLG contains only its linear absorption. Thus, the DKS returns to the central position of the pulsed pump. Our simulation results indicate that the location of DKS will be influenced by relaxation time τ_R . Meanwhile, the longer τ_R of the graphene results in lower peak power and wider pulse duration at a given pump pulse power.

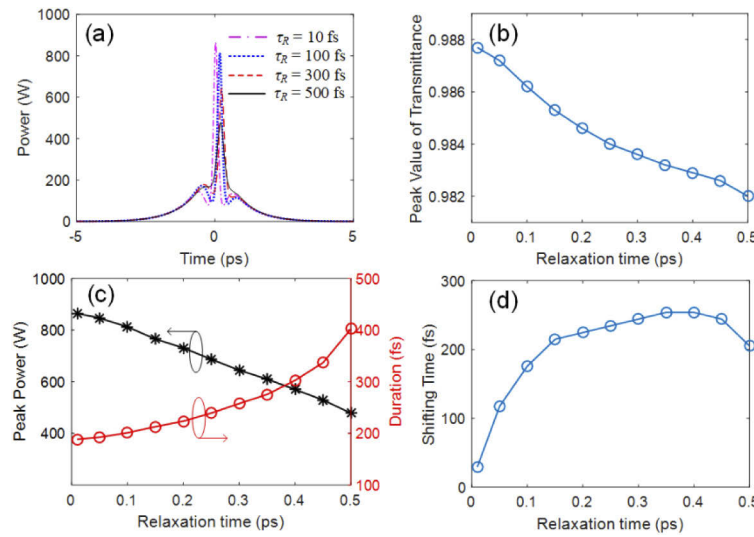


Fig. 10. (a) Temporal waveforms at different relaxation times of 10 fs, 100 fs, 300 fs and 500 fs. (b) The peak value of the SLG transmittance versus different relaxation time. (c) The peak power and duration of the generated DKS at different relaxation times. (d) The temporal location of the soliton with various relaxation times. Pump pulse: peak power 40 W, pulse duration 1.5 ps.

4. Conclusions

In conclusion, we have proposed a SLG-assisted FP microresonator which enables the deterministic generation of a single soliton without the requirement of pump frequency tuning. When the cavity is driven by pulsed pump with a proper fixed frequency, the intracavity field can directly evolve into a single-soliton state. The proposed microresonator is sufficiently robust to maintain the single-soliton state under various pump perturbations. The device properties, including the soliton region, influence of thermal tuning and graphene parameters, have been thoroughly investigated. Moreover, we believe that this device could be a new nonlinear platform bridging novel microresonators and well-known SA assisted mode locking due to the existence of graphene, and therefore promote fundamental research in nonlinear optics as well as facilitate practical applications of microresonator-based DKS.

Appendix A

In this appendix, we deduce the Lugiato-Lefever equation (LLE) for Fabry-Pérot (FP) microresonator from its equivalent coupled mode equation (CME). The FP-LLE we have derived is consistent with the results of the Ref. [39]. Besides, we verify the correctness of the developed LLE by comparing the simulation results demonstrated in [15].

A1. LLE derivation for the Kerr nonlinear FP resonator

Compared with ring microresonator, the co- and counter-propagation fields of FP resonator will interact and introduce an additional phase shift [15]. The field evolution of FP resonator has been theoretically analyzed by coupled mode equation in [15], and given by

$$\frac{\partial a_\mu}{\partial \tau} = - \left[1 + i\zeta_\mu - 2i \sum_{\mu'} |a_{\mu'}|^2 \right] a_\mu + i \sum_{\mu', \mu''} a_{\mu'} a_{\mu''} a_{\mu'+\mu''-\mu}^* + \delta_{0\mu} f \quad (8)$$

where μ is the mode number of Kerr combs, a_μ is the amplitude of μ -th mode, $\tau = \kappa T/2$ is the normalized time and κ is cavity decay rate [9]. The cavity decay rate κ is given by $\kappa = \kappa_{int} + \kappa_{ext}$, where κ_{int} is the intracavity decay rate, and κ_{ext} is the coupling rate. The ratio of $\eta = \kappa_{ext}/\kappa$ is coupling efficiency. When $\eta = 1/2$, the Kerr microresonator operates at critically coupled condition [9]. $\zeta_\mu = 2(\omega_\mu - \omega_p - \mu D_1)/\kappa$ describes the detuning frequency between central driving mode and resonance, and $\omega_\mu = \omega_0 + \mu D_1 + D_2 \mu^2/2$, where ω_0 is resonance frequency near the driving mode ω_p , $D_1 = 2\pi c/(n_0 L) = \omega_{FSR}$ is the free spectral range (FSR) of resonator (c is the speed of light, n_0 is refractive index, L is cavity length), and $D_2 = -D_1^2 \beta_2 c/n_0$ is the second-order cavity dispersion (β_2 is group-velocity dispersion) [8]. The amplitude of pump laser is given by $f = \sqrt{8\kappa_{ext}gP/(\kappa^3\hbar\omega_p)}$, where $g = \hbar\omega_p^2 n_2 D_1/(2\pi n_0 A_{eff})$ is the nonlinear coupling coefficient, which describes the resonance frequency shift in the Kerr nonlinear medium with the nonlinear refractive index n_2 , and effective mode area A_{eff} [15]. P is the power of driving laser, and \hbar is the Plank constant. $\delta_{0\mu}$ is the delta function that equals to 1 when $\mu = 0$, and otherwise equals to 0. In Eq. (8), the third term on the right side describes the additional phase shift in FP resonator, and the fourth term describes the parametric frequency conversion in $\chi^{(3)}$ -nonlinear medium. We rewrite Eq. (8) in a de-normalized form, given by

$$\frac{\partial A_\mu}{\partial T} = -\frac{\kappa}{2}A_\mu - i(\varpi_0 - \varpi_p + D_2 \mu^2/2)A_\mu + 2ig \sum_{\mu'} |A_{\mu'}|^2 A_\mu + ig \sum_{\mu', \mu''} A_{\mu'} A_{\mu''} A_{\mu'+\mu''-\mu}^* + \delta_{0\mu} \sqrt{\frac{P\kappa_{ext}}{\hbar\varpi_p}} \quad (9)$$

where we have introduced $T = 2\tau/\kappa$ and $A_\mu = a_\mu \sqrt{2g/\kappa}$, $|A_\mu|^2$ corresponds to the total photon number in mode μ . According to Fourier series expansion, The temporal slowly varying envelop of the intracavity field $A(T, t)$ can be written as

$$A(T, t) = \sum_{\mu} A_{\mu}(T) \exp(-i\mu\omega_{FSR}t) \quad (10)$$

where $t \in [-t_R/2, t_R/2]$ denotes the fast time in one resonator roundtrip, and t_R is the roundtrip time. From Eq. (10), we can obtain its differential equation about t and T , given by

$$\frac{\partial A}{\partial T} = \sum_{\mu} \frac{\partial A_{\mu}}{\partial T} \exp(-i\mu\omega_{FSR}t) \quad (11)$$

$$\frac{\partial^n A}{\partial t^n} = \sum_{\mu} (-i\mu\omega_{FSR})^n A_{\mu} \exp(-i\mu\omega_{FSR}t) \quad (12)$$

In Eq. (11), the $\partial A_{\mu}/\partial T$ term is given by Eq. (9), and using Eq. (12) to simplify the D_2 term ($D_2 = -\omega_{FSR}^2 \beta_2 c/n_0$), thus the Eq. (11) can be rewritten as

$$\begin{aligned} \frac{\partial A}{\partial T} = & \sum_{\mu} \left[-\frac{\kappa}{2}A_{\mu} - i(\varpi_0 - \varpi_p)A_{\mu} + 2ig \sum_{\mu'} |A_{\mu'}|^2 A_{\mu} + ig \sum_{\mu', \mu''} A_{\mu'} A_{\mu''} A_{\mu'+\mu''-\mu}^* \right] \exp(-i\mu\omega_{FSR}t) \\ & - i \frac{\beta_2 c}{2n_0} \frac{\partial^2 A}{\partial t^2} + \sqrt{\frac{P\kappa_{ext}}{\hbar\varpi_p}} \end{aligned} \quad (13)$$

According to the Parseval's theorem for continuous time Fourier series (CTFS), the $\sum_{\mu'} |A_{\mu'}|^2$ term is given by $\sum_{\mu'} |A_{\mu'}|^2 = \frac{1}{t_R} \int_{-t_R/2}^{t_R/2} |A(t)|^2 dt$ where $|A(t)|^2$ denotes the normalized power in

resonator. Through the CTFS transformation, the Eq. (13) can be rewritten as

$$\frac{\partial A}{\partial T} = \left[-\frac{\kappa}{2} - i(\varpi_0 - \varpi_p) + 2ig \frac{1}{t_R} \int_{-t_R/2}^{t_R/2} |A(t)|^2 dt + ig|A(t)|^2 - i\frac{\beta_2 c}{2n_0} \frac{\partial^2}{\partial t^2} \right] A + \sqrt{\frac{P\kappa_{ext}}{\hbar\varpi_p}} \quad (14)$$

Finally, Eq. (14) can be rewritten in the form of de-normalized LLE, and given by

$$t_R \frac{\partial E(T, t)}{\partial T} = \left[-\frac{\alpha}{2} - i\delta_0 + 2iL\gamma P_{cav} + iL\gamma|E|^2 - iL \frac{\beta_2}{2} \frac{\partial^2}{\partial t^2} \right] E + \sqrt{\theta} E_{in} \quad (15)$$

where $E(t) = \sqrt{(\hbar\omega_p)/t_R} A(t)$ is the field envelopes inside the cavity, $\alpha = \kappa t_R$ is the intracavity total loss, $\delta_0 = (\omega_0 - \omega_p)t_R$ is the pump-resonance detuning, $\gamma = \omega_p n_2 / (A_{eff} c)$ is the nonlinear coefficient, $\theta = \kappa_{ext} t_R$ is the pump coupling coefficient, $E_{in} = \sqrt{P}$ is the driving field, P_{cav} is the average power accumulated in the cavity, and given by

$$P_{cav} = \frac{1}{t_R} \int_{-t_R/2}^{t_R/2} |E|^2 dt \quad (16)$$

A2. LLE verification

To verify the correctness of deduced LLE in Eq. (15), we compare simulation results of the deduced LLE and CME used in [15]. The simulated FP microresonator has a resonance width $\kappa/2\pi = 7$ MHz, FSR $\omega_{FSR}/2\pi = 10$ GHz, nonlinear refractive index $n_2 = 2.6 \text{ m}^2\text{W}^{-1}$, effective mode area $A_{eff} = 85 \mu\text{m}^2$, group-velocity dispersion $\beta_2 = -20 \text{ ps}^2\text{km}^{-1}$. The parameter of FP microresonator is consistent with [15], except the FSR is set to 10 GHz rather than 9.77 GHz for simplification. The synchronous driving field is characterized by 41 frequency combs with equal phase and power, and the total power is 75 mW. The noise with maximum amplitude of 1×10^{-8}

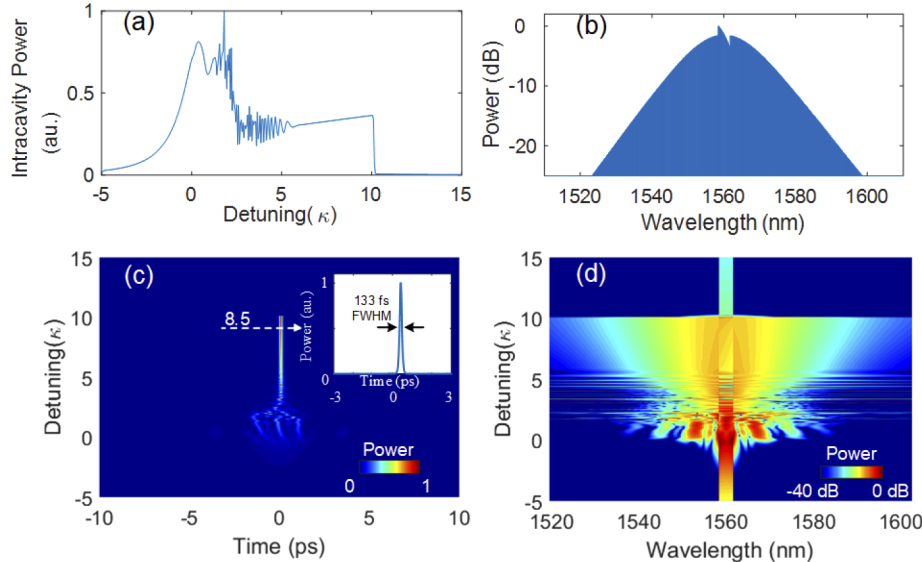


Fig. 11. (a) Intracavity power evolution when the pump-resonance detuning is scanned from -5κ to 15κ . (b) The spectrum of single soliton when the field is stabilized at 8.5κ . (c) Temporal evolution of intracavity power when the driving mode is tuned across the resonance. Inset: temporal waveform at the detuning of 8.5κ . (d) Spectral evolution of intracavity power with same detuning range

and random phase is added to the pump field to excite any potential instability. Equation (16) is solved by split-step Fourier method [13,16], and the pump-resonance detuning is normalized with κ . The simulation results are presented in Fig. 11, and coincide with the simulation results of [15]. Figure 11(a) demonstrates the intracavity power variation versus the pump-resonance detuning, and the curve exhibits single soliton step from 5.5κ to 10κ . Figure 10(b) shows the single-soliton spectrum when intracavity field is stabilized at the detuning of 8.5κ . The spectrum exhibits the characteristics of smooth sech²-envelope, and the -25dB spectral width is around 80nm, in agreement with [15]. The temporal and spectral evolution of intracavity power are shown in Figs. 11(c) and 11(d). The noise evolution pattern has slightly difference compared with [15], which is cause by random phase noise in driving pulse. The temporal waveform at the detuning of 8.5κ is shown at the inset of Fig. 11(c) with a duration of 133fs (FWHM).

In conclusion, our simulation results from the deduced LLE are in good agreement with the simulation results solved from CME, which verifies the correctness of formula derivation.

Funding

National Natural Science Foundation of China (61922056, 61875122, 61535006).

Disclosures

The authors declare no conflicts of interest.

References

1. A. Pasquazi, M. Peccianti, L. Razzari, D. J. Moss, S. Coen, M. Erkintalo, Y. K. Chembo, T. Hansson, S. Wabnitz, P. Del'Haye, X. Xue, A. M. Weiner, and R. Morandotti, "Micro-combs: A novel generation of optical sources," *Phys. Rep.* **729**, 1–81 (2018).
2. K. Y. Yang, K. Beha, D. C. Cole, X. Yi, P. Del'Haye, H. Lee, J. Li, D. Y. Oh, S. A. Diddams, S. B. Papp, and K. J. Vahala, "Broadband dispersion-engineered microresonator on a chip," *Nat. Photonics* **10**(5), 316–320 (2016).
3. P. Marin-Palomo, J. N. Kemal, M. Karpov, A. Kordts, J. Pfeifle, M. H. P. Pfeiffer, P. Trocha, S. Wolf, V. Brasch, M. H. Anderson, R. Rosenberger, K. Vijayan, W. Freude, T. J. Kippenberg, and C. Koos, "Microresonator-based solitons for massively parallel coherent optical communications," *Nature* **546**(7657), 274–279 (2017).
4. S. B. Papp, K. Beha, P. Del'Haye, F. Quinlan, H. Lee, K. J. Vahala, and S. A. Diddams, "Microresonator frequency comb optical clock," *Optica* **1**(1), 10–14 (2014).
5. D. T. Spencer, T. Drake, T. C. Briles, J. Stone, L. C. Sinclair, C. Fredrick, Q. Li, D. Westly, B. R. Ilic, A. Bluestone, N. Volet, T. Komljenovic, L. Chang, S. H. Lee, D. Y. Oh, M.-G. Suh, K. Y. Yang, M. H. P. Pfeiffer, T. J. Kippenberg, E. Norberg, L. Theogarajan, K. Vahala, N. R. Newbury, K. Srinivasan, J. E. Bowers, S. A. Diddams, and S. B. Papp, "An optical-frequency synthesizer using integrated photonics," *Nature* **557**(7703), 81–85 (2018).
6. A. Dutt, C. Joshi, X. Ji, J. Cardenas, Y. Okawachi, K. Luke, A. L. Gaeta, and M. Lipson, "On-chip dual-comb source for spectroscopy," *Sci. Adv.* **4**(3), e1701858 (2018).
7. P. Trocha, M. Karpov, D. Ganin, M. H. P. Pfeiffer, A. Kordts, S. Wolf, J. Krockenberger, P. Marin-Palomo, C. Weimann, S. Randel, W. Freude, T. J. Kippenberg, and C. Koos, "Ultrafast optical ranging using microresonator soliton frequency combs," *Science* **359**(6378), 887–891 (2018).
8. T. Herr, V. Brasch, J. D. Jost, I. Mirgorodskiy, G. Lihachev, M. L. Gorodetsky, and T. J. Kippenberg, "Mode spectrum and temporal soliton formation in optical microresonators," *Phys. Rev. Lett.* **113**(12), 123901 (2014).
9. T. Herr, V. Brasch, J. D. Jost, C. Y. Wang, N. M. Kondratiiev, M. L. Gorodetsky, and T. J. Kippenberg, "Temporal solitons in optical microresonators," *Nat. Photonics* **8**(2), 145–152 (2014).
10. X. Yi, Q.-F. Yang, K. Y. Yang, M.-G. Suh, and K. Vahala, "Soliton frequency comb at microwave rates in a high-Q silica microresonator," *Optica* **2**(12), 1078–1085 (2015).
11. T. J. Kippenberg, R. Holzwarth, and S. A. Diddams, "Microresonator-based optical frequency combs," *Science* **332**(6029), 555–559 (2011).
12. T. J. Kippenberg, A. L. Gaeta, M. Lipson, and M. L. Gorodetsky, "Dissipative Kerr solitons in optical microresonators," *Science* **361**(6402), eaan8083 (2018).
13. M. R. E. Lamont, Y. Okawachi, and A. L. Gaeta, "Route to stabilized ultrabroadband microresonator-based frequency combs," *Opt. Lett.* **38**(18), 3478–3481 (2013).
14. C. Bao, Y. Xuan, J. A. Jaramillo-Villegas, D. E. Leaird, M. Qi, and A. M. Weiner, "Direct soliton generation in microresonators," *Opt. Lett.* **42**(13), 2519–2522 (2017).
15. E. Obrzud, S. Lecomte, and T. Herr, "Temporal solitons in microresonators driven by optical pulses," *Nat. Photonics* **11**(9), 600–607 (2017).

16. S. Coen, H. G. Randle, T. Sylvestre, and M. Erkintalo, "Modeling of octave-spanning Kerr frequency combs using a generalized mean field Lugiato Lefever model," *Opt. Lett.* **38**(1), 37–39 (2013).
17. H. Guo, M. Karpov, E. Lucas, A. Kordts, M. H. P. Pfeiffer, V. Brasch, G. Lihachev, V. E. Lobanov, M. L. Gorodetsky, and T. J. Kippenberg, "Universal dynamics and deterministic switching of dissipative Kerr solitons in optical microresonators," *Nat. Phys.* **13**(1), 94–102 (2017).
18. X. Yi, Q.-F. Yang, K. Youl Yang, and K. Vahala, "Active capture and stabilization of temporal solitons in microresonators," *Opt. Lett.* **41**(9), 2037–2040 (2016).
19. V. Brasch, M. Geiselmann, T. Herr, G. Lihachev, M. H. P. Pfeiffer, M. L. Gorodetsky, and T. J. Kippenberg, "Photonic chip-based optical frequency comb using soliton Cherenkov radiation," *Science* **351**(6271), 357–360 (2016).
20. V. Brasch, M. Geiselmann, M. H. P. Pfeiffer, and T. J. Kippenberg, "Bringing short-lived dissipative Kerr soliton states in microresonators into a steady state," *Opt. Express* **24**(25), 29312–29320 (2016).
21. H. Zhou, Y. Geng, W. Cui, S.-W. Huang, Q. Zhou, K. Qiu, and C. Wei Wong, "Soliton bursts and deterministic dissipative Kerr soliton generation in auxiliary-assisted microcavities," *Light: Sci. Appl.* **8**(1), 50 (2019).
22. C. Joshi, J. K. Jang, K. Luke, X. Ji, S. A. Miller, A. Klenner, Y. Okawachi, M. Lipson, and A. L. Gaeta, "Thermally controlled comb generation and soliton modelocking in microresonators," *Opt. Lett.* **41**(11), 2565–2568 (2016).
23. D. C. Cole, J. R. Stone, M. Erkintalo, K. Y. Yang, X. Yi, K. J. Vahala, and S. B. Papp, "Kerr-microresonator solitons from a chirped background," *Optica* **5**(10), 1304–1310 (2018).
24. T. Kumagai, N. Hirota, K. Sato, K. Namiki, H. Maki, and T. Tanabe, "Saturable absorption by carbon nanotubes on silica microtoroids," *J. Appl. Phys.* **123**(23), 233104 (2018).
25. R. Imamura, S. Fujii, T. S. L. Prugger Suzuki, R. Suzuki, R. Ishida, M. Ito, H. Maki, L. Yang, and T. Tanabe, "Saturable absorption with CNT coupled WGM and fabrication of Er-doped microresonator for on-chip mode-locked laser," in *CLEO: OSA Technical Digest* (Optical Society of America, 2019), p. ck_3_5.
26. A. Martinez and S. Yamashita, "10 GHz fundamental mode fiber laser using a graphene saturable absorber," *Appl. Phys. Lett.* **101**(4), 041118 (2012).
27. B. Yao, S.-W. Huang, Y. Liu, A. K. Vinod, C. Choi, M. Hoff, Y. Li, M. Yu, Z. Feng, D.-L. Kwong, Y. Huang, Y. Rao, X. Duan, and C. W. Wong, "Gate-tunable frequency combs in graphene–nitride microresonators," *Nature* **558**(7710), 410–414 (2018).
28. D. K. Serkland, G. D. Bartolini, A. Agarwal, P. Kumar, and W. L. Kath, "Pulsed degenerate optical parametric oscillator based on a nonlinear-fiber Sagnac interferometer," *Opt. Lett.* **23**(10), 795–797 (1998).
29. J. Lasri, P. Devgan, T. Renyong, J. E. Sharping, and P. Kumar, "A microstructure-fiber-based 10-GHz synchronized tunable optical parametric oscillator in the 1550-nm regime," *IEEE Photonics Technol. Lett.* **15**(8), 1058–1060 (2003).
30. G. Xing, H. Guo, X. Zhang, T. C. Sum, and C. H. A. Huan, "The physics of ultrafast saturable absorption in graphene," *Opt. Express* **18**(5), 4564–4573 (2010).
31. M. Breusing, S. Kuehn, T. Winzer, E. Malić, F. Milde, N. Severin, J. P. Rabe, C. Ropers, A. Knorr, and T. Elsaesser, "Ultrafast nonequilibrium carrier dynamics in a single graphene layer," *Phys. Rev. B* **83**(15), 153410 (2011).
32. W. B. Cho, J. W. Kim, H. W. Lee, S. Bae, B. H. Hong, S. Y. Choi, I. H. Baek, K. Kim, D.-I. Yeom, and F. Rotermund, "High-quality, large-area monolayer graphene for efficient bulk laser mode-locking near 1.25 μm," *Opt. Lett.* **36**(20), 4089–4091 (2011).
33. V. Brasch, E. Obrzud, S. Lecomte, and T. Herr, "Noise filtering in synchronously-driven Kerr frequency combs," in *CLEO: OSA Technical Digest* (Optical Society of America, 2019), p. STh4J.1.
34. F. Leo, L. Gelens, P. Emplit, M. Haelterman, and S. Coen, "Dynamics of one-dimensional Kerr cavity solitons," *Opt. Express* **21**(7), 9180–9191 (2013).
35. I. V. Barashenkov and Y. S. Smirnov, "Existence and stability chart for the ac-driven, damped nonlinear Schrödinger solitons," *Phys. Rev. E* **54**(5), 5707–5725 (1996).
36. P. Parra-Rivas, D. Gomila, M. A. Matfàs, S. Coen, and L. Gelens, "Dynamics of localized and patterned structures in the Lugiato-Lefever equation determine the stability and shape of optical frequency combs," *Phys. Rev. A* **89**(4), 043813 (2014).
37. E. Lucas, M. Karpov, H. Guo, M. L. Gorodetsky, and T. J. Kippenberg, "Breathing dissipative solitons in optical microresonators," *Nat. Commun.* **8**(1), 736 (2017).
38. A. A. Balandin, S. Ghosh, W. Bao, I. Calizo, D. Teweldebrhan, F. Miao, and C. N. Lau, "Superior thermal conductivity of single-layer graphene," *Nano Lett.* **8**(3), 902–907 (2008).
39. D. C. Cole, A. Gatti, S. B. Papp, F. Prati, and L. Lugiato, "Theory of Kerr frequency combs in Fabry-Perot resonators," *Phys. Rev. A* **98**(1), 013831 (2018).